INT. J. NUM. METH. HEAT FLUID FLOW, VOL. 6, 19–34 (1996)

COMPUTATION OF ISOTHERMAL AND REACTING FLOWS IN TURBOJET AFTERBURNERS

M. RAVICHANDRAN AND V. GANESAN

Department of Mechanical Engineering, Indian Institute of Technology, Madras 600 036, India

ABSTRACT

Computations have been made of the three-dimensional flow field development, chemical reaction and combustion processes in a typical turbojet afterburner system under both isothermal and reacting flow conditions. The calculations are based upon a numerical solution of the time-averaged transport equations for mass, momentum, turbulence kinetic energy, dissipation rate, enthalpy and species concentrations using a finite-volume formulation. The physical models include the k–ε turbulence model, the eddy break-up model, a two-step reaction model, a droplet vaporization and combustion model and a six-flux radiation model. The mean flow structures are presented in important longitudinal and cross-sectional planes which show certain striking similarities and contrasting differences for isothermal and reacting flows. The flame stabilizer flow is shown to be dominanted by a complex combination of recirculation and vortex patterns. Combustion alters convergence and mixing flow patterns downstream of the flame stabilizer, thus influencing the selection of the fuel injection system. The predicted reacting flow parameters identify a number of design parameters such as fuel injector location, high degree reaction zone, nozzle opening area and the corresponding fuel flow rate.

KEY WORDS Reacting flows Combination k–ε turbulence model Finite volume

NOMENCLATURE

a	Coupling coefficient for finite difference equations
C_μ, C_1, C_2	Constants in the turbulence model
C_p	Specific heat of gaseous mixture at constant pressure
$C_{p,i}$	Specific heat for the species i
C_{EBU}	Constant in the eddy-breakup model
a_i, b_i, c_i, d_i, e_i	Constants used in the specific heat calculation for species i
E_1, E_2	Arrhenius reaction rate constants for unburnt fuel and carbon monoxide
f	Mixture fraction
f_j	Mass fraction of the droplet of jth size range
$\bar{h}$	Stagnation enthalpy
h	Enthalpy
H_{fu}	Heat of reaction
k	Kinetic energy of turbulence
m	Mass of droplet in the size range s and $s+ds$
m_{co}	Mass fraction of carbon monoxide
m_{fu}	Mass fraction of unburnt fuel
m_i	Mass fraction of the species i
S_u, S_p	Source terms
S_ϕ	Source terms in the governing differential equations for the variable ϕ
T	Temperature
u, v, w	Predicted time-averaged velocities in the axial, radial and tangential directions, respectively
x, r, θ	Distances in the axial, radial and tangential directions, respectively
Z_{fu}, Z_{co}	Constants in the Arrhenius reaction rate unburnt fuel and carbon monoxide, respectively
β	Either the mixture density or zero in the governing differential equations for gas
ρ	Mixture density
ρ_d	Droplet density
ε	Dissipation rate
ϕ	Dependent variable in the governing differential equations
Γ_ϕ	Appropriate exchange coefficient for the variable ϕ
μ_{eff}	Effective viscosity
μ_t	Turbulent viscosity

0961–5539/96/030019–16$2.00

Received February 1994
Revised May 1995

M	Mass of a single droplet
M_i	Molecular weight of the species i
M_{max}	Mixture molecular weight
p	Pressure
R	Gas constant
R^x, R^r, R^θ	Radiation fluxes in the axial, radial and tangential directions, respectively
s	Characteristic droplet size for size range j
σ	Effective Prandtl/Schmidt number
δ	Distance of the near-wall point to the wall

Abbreviations

BRG	Bottom Ring Gutter
RC	Recirculation
RG	Radial Gutter
TKE	Turbulence Kinetic Energy
TRG	Top Ring Gutter

INTRODUCTION

Afterburners are mainly used for augmenting the basic thrust in military aircrafts and cruise missiles during take-off or for a short period of acceleration, and are most indispensable to the engines of supersonic aircrafts. The mixing of fuel and air streams occurs in a turbulent flow field formed by flow of two streams in the afterburner. A detailed understanding of the aerodynamic and fuel-air mixing process in such a configuration is necessary for improving the combustion efficiency and thrust developed by the afterburner. Practical afterburner geometries are often very complex, including two phase flow phenomema, evaporation and heat transfer, chemical kinetics and turbulence all occurring simultaneously. The recirculation regions and the corresponding shear layers behind the flame stabilizer are characterized by intense turbulence and mixing phenomena. Very little is known about the turbulence-chemistry interactions in such a complex three-dimensional flow field. In addition, the combustor effluent which enters the afterburner has a composition that could significantly influence transient processes such as ignition and flame blowout.

There have been very few studies, experimental or analytical, of the detailed flow and combustion processes inside practical afterburner systems. Reacting flow tests in practical afterburners[1,2] are aimed primarily at acquiring only the gross features of performance parameters like combustion efficiency, pressure loss, combustion instability, etc. The majority of earlier numerical studies have concentrated on simple bluff bodies[3,4] like disks, cones and spheres, mainly due to their simplicity and the availability of experimental data. Lee and Lin[5] employed a zonal grid method in the computation of 2-D cold flows over both a disk in a pipe and a two-ring conical flame stabilizer. The flow predictions behind a disk were in good agreement with available experimental data; however, for the flame stabilizer, they suffered from lack of experimental data for validation. The numerical predictions in practical afterburners have been mostly two-dimensional and confined to simple systems having one of the components, such as an annular diffuser or flame stabilizer, which is either of the single or two-ring type. Elgobashi *et al.*[6] predicted the chemically reacting flow properties in a simple V-gutter jet engine afterburner and discussed the complications of modelling of the buzz phenomenon due to the interaction between turbulence and combustion. Lixing and Jian[7] simulated reacting flows in afterburners and compared their predictions with experiments; unfortunately, they restricted their attention to the diffuser part only, leaving out the flame stabilizer. Reacting flow predictions[8] for a turbofan afterburner (with core and bypass flow) have also been made, again with a simple conical flame stabilizer. Chuang and Jiang[9] made numerical predictions of an afterburner, consisting of an annular diffuser and a two-ring flame stabilizer, as a function of the air-fuel ratio using a diffusion flame analysis.

Aircraft engine afterburners are indeed quite complex and comprise several interconnected parts. The study of flow fields past either one of the components such as the above might not be sufficient to understand the interaction of other parts on the flow patterns. Also, the flame stabilizers used in practical afterburners might be combinations of ring and radial gutters and, in such ases, the flow becomes three-dimensional involving circumferential non-uniformities and transport, as seen from the water visualization studies of Isaac *et al.*[10]. Hence, a typical afterburner

system consisting of an annular diffuser, a flame stabilizer and a variable area nozzle, has been selected here (*Figure 1*) for the numerical analysis. The flame stabilizer is a combination of a bottom ring V-gutter (BRG) and a top ring V-gutter (TRG) of about 35° included angle each and with four radial V-gutters (RG) of 45° included angle. Film cooling slots are introduced only at three axial stations because of the absence of exact details in the literature (size, shape, location and number). Since the duration period of thrust augmentation is short and afterburners form a permanent integral part of aircraft engines, isothermal flow field analysis has been separately made to understand the flow patterns during long non-afterburning periods in aircrafts. The comprehensive reacting flow analysis has also been made in the same geometry with the variable area nozzle in fully open conditions.

MATHEMATICAL ANALYSIS

The calculations presented here have been obtained by solving the full three-dimensional equations for conservation of mass, linear momentum, enthalpy and species concentrations in time-averaged form. The general form of the equation for steady, incompressible, turbulent flow can be written as,

$$\frac{1}{r}\left\{\left[\frac{\partial}{\partial x}(\beta u r\phi)+\frac{\partial}{\partial r}(\beta v r\phi)+\frac{\partial}{\partial \theta}(\beta w\phi)\right]-\left[\frac{\partial}{\partial x}\left(r\Gamma_\phi\frac{\partial \phi}{\partial x}\right)+\frac{\partial \phi}{\partial r}\right)+\frac{\partial}{\partial \theta}\left(\Gamma_\phi\frac{\partial \phi}{r\,\partial \theta}\right)\right]\right\}=S_\phi \quad (1)$$

and the details of the terms in the various equations are given in *Table 1*. The first six partial differential equations of *Table 1* are solved for isothermal flows and all the equations are solved for reacting flows.

The turbulent shear stresses are calculated using the k–ε model of Launder and Spalding[11]. The turbulent viscosity is calculated from,

$$\mu_t = C_\mu \rho k^2/\varepsilon \quad (2)$$

and the model contains five empirical constants which are assigned the following values:

$$C_\mu = 0.09, \quad C_1 = 1.43, \quad C_2 = 1.92, \quad \sigma_k = 0.9, \quad \sigma_\varepsilon = 1.3.$$

The chemical reaction between fuel (kerosene) and air is modeled by a two-step kinetics mechanism in which each component of the fuel reacts separately with oxidizer to form intially CO and then CO_2 (two-step reaction model).

$$C_xH_y + 1/2(x+y/2)O_2 \rightarrow xCO + (y/2)H_2O \quad (3)$$

$$xCO + (x/2)O_2 \rightarrow xCO_2 \quad (4)$$

The reaction rates for the m_{fu} and m_{co} equations are determined by taking into account the minimum of either the reaction rate obtained from the eddy break-up model of Spalding[12] or

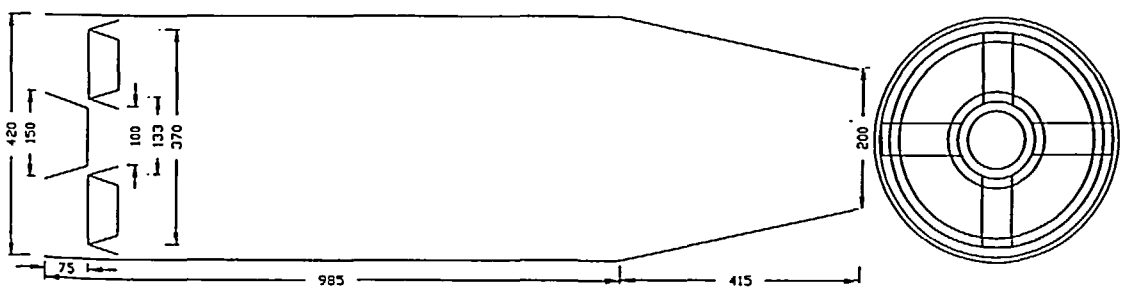

Figure 1 Aircraft afterburner geometry

Table I Values of ϕ, β, Γ_ψ and S_ψ

Equation	ϕ	β	Γ	S_ψ
Continuity	l	ρ	0	0
x-momentum	u	ρ	μ	$-\frac{\partial p}{\partial x}+\frac{\partial}{\partial x}\left(\mu\frac{\partial u}{\partial x}\right)+\frac{1}{r}\frac{\partial}{\partial r}\left(r\mu\frac{\partial v}{\partial x}\right)+\frac{1}{r}\frac{\partial}{\partial \theta}\left(\mu\frac{\partial w}{\partial x}\right)$
r-momentum	v	ρ	μ	$-\frac{\partial p}{\partial r}+\frac{\partial}{\partial x}\left(\mu\frac{\partial u}{\partial r}\right)+\frac{1}{r}\frac{\partial}{\partial r}\left(r\mu\frac{\partial y}{\partial r}\right)+\frac{1}{r}\frac{\partial}{\partial \theta}\left(\mu\frac{\partial w}{\partial r}-\frac{w}{r}\right)+\frac{\rho w^2}{r}-\frac{2\mu}{r}\left(\frac{\partial w}{r\,\partial \theta}+\frac{v}{r}\right)$
θ-momentum	w	ρ	μ	$-\frac{1}{r}\frac{\partial p}{\partial \theta}+\frac{\partial}{\partial x}\left(\frac{\mu}{r}\frac{\partial u}{\partial \theta}\right)+\frac{1}{r}\frac{\partial}{\partial r}\left[\mu r\left(\frac{1}{r}\frac{\partial v}{\partial \theta}-\frac{w}{r}\right)\right]-\frac{\rho v w}{r}+\frac{1}{r}\frac{\partial}{\partial \theta}\frac{\mu}{r}\left(\frac{\partial w}{\partial \theta}+2v\right)+\frac{\mu}{r}\left(\frac{\partial w}{\partial r}+\frac{\partial v}{r\,\partial \theta}-\frac{w}{r}\right)$
Turbulence kinetic energy	k	ρ	$\frac{\mu_{eff}}{\sigma_{keff}}$	$G_k^+-C_p\varepsilon\rho$
Energy dissipation rate	ε	ρ	$\frac{\mu_{eff}}{\sigma_{geff}}$	$(C_1G_k-C_2\rho\varepsilon)\frac{\varepsilon}{k}$
Fuel mass fraction	$\dot{m}_{fu}$	ρ	$\frac{\mu}{\rho_{fu}}$	(1) $-Z_{fu}\rho^2 m_{fu}m_{ox}e^{-k_{fu}/RT}$ [Arrhenius reaction] (2) $-C_{EBU}m_{fu}\rho\frac{\varepsilon}{k}$ [Eddy-breakup model]
CO mass fraction	m_{CO}	ρ	$\frac{\mu}{\sigma_{CO}}$	(1) $-Z_{CO}\rho^2 m_{CO}m_{CO}e^{-k_{CO}/RT}$ [Arrhenius reaction] (2) $-C_{EBU}m_{CO}\rho\frac{\varepsilon}{k}$ [Eddy-breakup model]
Mixture fraction	f	ρ	$\frac{\mu}{\sigma_k}$	0
Stagnation enthalpy	h	ρ	$\frac{\mu}{\sigma_k}$	(1) 0 if no radiation (2) $2a(R^x+R^y-R^z-3E)$ if radiation is included
x-direction radiation flux	R^x	0	$\frac{1}{a+s}$	$-\frac{1}{r}\left[\frac{\partial}{\partial r}\left(\frac{r}{a+s}\frac{\partial R^x}{\partial r}\right)+\frac{\partial}{\partial \theta}\left(\frac{1}{a+s}-\frac{1}{r}\frac{\partial R^x}{\partial \theta}\right)\right]-\left[a(R^x-E)+\frac{s}{3}(2R^x-R^y-R^z)\right]$
r-direction radiation flux	R^y	0	$\frac{1}{a+s+1/r}$	$-\frac{\partial}{\partial x}\left(\frac{1}{a+s+1/r}\frac{\partial R^y}{\partial x}\right)-\frac{1}{r}\frac{\partial}{\partial \theta}\left(\frac{1}{a+s+1/r}\frac{\partial R^y}{r\,\partial \theta}\right)-\left[a(R^y-E)+\frac{s}{3}(2R^y-R^x-R^z)\right]$
θ-direction radiation flux	R^z	0	$\frac{1}{a+s}$	$-\frac{\partial}{\partial x}\left(\frac{1}{a+s}\frac{\partial R^z}{\partial x}\right)-\frac{1}{r}\frac{\partial}{\partial r}\left(\frac{r}{a+s}\frac{\partial R^z}{\partial r}\right)-\left[a(R^z-E)+\frac{s}{3}(2R^z-R^x-R^y)\right]$

Table 1 Continued

Equation	ϕ	β	Γ	S_ϕ
Mass fraction of droplet of jth size	f_i	ρ	$\frac{\mu}{\sigma_{fl}}$	$\frac{\rho}{\rho^p}\ln(1+B)\left[\frac{f_{j-1}}{S_{j-1}-S_j}\frac{f_i}{S_j-S_{j+1}}-\frac{1.5f_j}{S_j}\right]$ for $j<k$ $\frac{\rho}{\rho p}\ln(1+B)\left[\frac{f_{k-1}}{S_{k-1}-S_k}-\frac{1.5f_k}{S_k}\right]$ for $j=k$ where $B=\frac{hG-hS}{L_{fg}}+\frac{m_{ox}}{L_{fg}}$

$$+G_k=\mu_t\left[2\left(\frac{\partial u}{\partial x}\right)^2+\left(\frac{\partial v}{\partial r}\right)^2+\left(\frac{\partial w}{r\partial\theta}+\frac{v}{r}\right)^2+\left(\frac{\partial w}{\partial x}+\frac{\partial u}{r\partial\theta}\right)^2+\left(\frac{\partial u}{\partial r}+\frac{\partial v}{\partial x}\right)^2+\left(\frac{\partial w}{\partial r}+\frac{\partial v}{r\partial\theta}-\frac{w}{r}\right)^2\right]$$

The source terms that contain div v conditions are neglected

the Arrhenius reaction rate. The injected fuel is assumed to be in the form of droplets of various sizes (DS1, DS2, DS3, DS4 and DS5 corresponding to 50, 40, 30, 20 and 10 microns, respectively) and these droplets diminish in size in the course of their downstream motion. The diminution in size may be a result of either vaporization or direct oxidation, or both. The size of a droplet is characterized by the variable s which is taken to be the square of the droplet radius. Because of this simplification, this results in, namely, that the rate of change of size with time (i.e., $\dot{s}$) is a constant independent of s. Even though, this is a rather poor assumption from the point of view of droplet combustion modelling, it has been employed for its simplicity. Further, an elaborate model may require more computer memory and time.

A control-volume analysis involving a balance of the droplets entering and leaving and changing size, after integration over a size range s and $s+ds$ yields:

$$\frac{\mathrm{d}}{\mathrm{d}t}(\rho f_j)+\int_{s_{j+1}}^{s_j}\dot{s}\left(\frac{\partial m}{\partial s}-\frac{m}{M}\frac{\partial M}{\partial s}\right)ds=0 \tag{5}$$

The derivation of this equation assumes that droplets of finite size are neither created nor destroyed. The true variation of m with s at any particular location will normally be represented by a smooth curve. However, since a finite-difference scheme is employed in the calculations, the true distribution is replaced by a stepped one. The droplet sizes are arranged so that $j=1$ corresponds to the largest size and $j=k$ corresponds to the smallest size. The above equation may now be evaluated on the basis of the mass transfer rate and a presumed $m-s$ distribution and can be shown to be the source terms of the droplet equations as given in *Table 1*.

In the present calculations, a special form of the conservation equations based on energy involving $C_p(T)$ and T is employed. The specific heat of the mixture at constant pressure is given by,

$$C_p(T)=\sum_i m_i C_{p,i}(T) \tag{6}$$

with summation over all species. The variation of the specific heat with temperature is considered by using polymomials of the form,

$$C_{p,i}=a_i+b_iT+C_iT^2+d_iT^3+e_iT^4 \tag{7}$$

Stagnation enthalpy is defined as:

$$\bar{h}=h+\frac{u^2+v^2+w^2}{2} \tag{8}$$

The specific enthalpy, 'h', is defined by,

$$h=\sum m_i\left(h_i+\int_{T_0}^{T} C_{p_i}\,\mathrm{d}T\right) \tag{9}$$

The partial differential equation for the enthalpy has been derived by assuming that the exchange coefficients for the transport of the mixture components and the exchange coefficient for heat conduction are all equal. The effects of radiation are accounted for by using a six-flux model of radiation. The above system of equations are complete with the following equation of state

$$p=\rho RT/M_{mix} \tag{10}$$

where

$$1/M_{mix}=\sum_i m_i/M_i \tag{11}$$

SOLUTION PROCEDURE

The solution of the above steady, three-dimensional coupled partial differential equations has been obtained using a finite-volume scheme. The formulation comprises a quasi-linearized, implicit, conservative scheme using hybrid differencing for convective fluxes. The use of higher order differencing scheme such as the QUICK algorithm would have helped to reduce false diffusion errors in the calculation of this complex 3-D flow. However, importance in the current work; further development would be required to allow a higher order scheme to be adopted within the framework of the complex flame stabilizer geometry treatment. Since the appearance of strong cross-stream diffusion which characterizes flame stabilizers is known to be pressure dominated, it seemed worthwhile beginning the calculations with a lower order of the convective discretization before proceeding to more complicated and numerically less stable techniques. The method is formulated in terms of velocity and pressure using a staggered grid arrangement. The pressure velocity coupling is handled via the standard SIMPLE pressure correction algorithm[13]. The general structure of the final finite difference equation is,

$$a_p\phi_p=\sum_n^M a_n\phi_n+S_u+S_p\phi_p \tag{12}$$

The above equation is solved by repeated alternate line sweeps in the three coordinate directions. At each line, a line Gaussian elimination algorithm (Thomas algorithm) is used. Underrelaxation factors are used for each iteration process to help the convergence of each calculation.

The solid walls (assumed to be infinitely thin) represent the real surface. Planar approximations are used to represent the solid walls which have been assumed infinite. Because of the non-availability of computer resources, the ladder-step approximation has to be attempted, though a grid generation will be more appropriate. Calculation of the intersection points between the surface and the staggered grids enables the identification of individual finite volume cells which lie inside or outside the flow region. For cells which intersect with the boundary, the intersection points are used to calculate the proportion of each of the six cell face areas which lie inside the flow region. The finite volume equations are then modified by taking these truncated or extended cell face areas into account. The step-wise variations in the cross-sectional area for introducing the film cooling air have been simulated by means of coefficient modifications in the various equations solved.

GRID DISTRIBUTION AND BOUNDARY CONDITIONS

The grid network used to discretize the turbojet afterburner geometry is shown in *Figure 2*. Flow symmetry and periodicity require a solution only for a sector formed by a 90° slice comprising

one radial gutter with symmetry boundary conditions along the edges of the sector. A grid consisting of $32 \times 28 \times 15$ nodes (13,440 nodes) in the x, r and θ directions, respectively, represented the cylindrical polar calculation domain for the afterburner flow region. The first stage of the calculations has also been performed with a relatively coarser mesh of 10,500 nodes (by changing the x-direction nodes only). The differences in the results between these two meshes are relatively minor (less than 3%) and suggest that the finer grid used for the calculations is acceptable. Still finer grids would represent the modeled geometry more accurately, but restrictions on availability of computer storage and time imposed difficulties in the mesh refinement process. The CPU time required for the isothermal and reacting flow calculations is 24 and 56 seconds per iteration respectively in an AT-486 machine. Typically, about 600 iterations are necessary to make the residuals decrease to the 0.01% level for both isothermal and reacting flows.

The boundary conditions for each dependent variable are specified at the four boundaries of the integration domain because the nature of the governing differential equations is predominantly elliptic. A uniform axial velocity profile of 150 m/s at a temperature of 900 K is assumed. Radial velocity is set equal to zero and swirl velocities are assumed to be 5% of the axial velocity (swirl ratio = 0.05) which varies linearly, i.e., zero at the centre to a maximum near the no-slip wall. The turbulence kinetic energy (TKE) is assumed to be 1% of the mean flow kinetic energy at that point. Inlet values for the length scale are assumed to be 10% of the characteristic port dimension, i.e., the difference between the inlet and outlet diameters. At the exit plane, the axial gradients of all the variables are assumed to be zero. At the centreline, radial gradients of the variables are assumed to be zero due to symmetry. The implementation of the boundary conditions at the solid wall is handled by standard wall functions[14]. The near boundary grid node is taken sufficiently far from the wall and the turbulent viscosity is used for all internal nodes. The shear stresses and other fluxes at the wall are specified. The shear stress at any point on the wall surface is expressed as a function of the near wall velocity components (V_P) locally parallel to the wall surface. The shear stress parallel to the wall fact may be written as

$$\tau_s = \Gamma_{wall} V_P \tag{13}$$

For the velocity components parallel to the wall, Γ_{wall} is calculated as:

for $y+ > 11.5$, $\mu_1 y^+ / [(1/VK)\delta \ln(Ey^+)]$;
for $y+ < 11.5$, μ_1/δ;

for smooth walls, $VK = 0.4$ and $E = 0.9$ and y^+ is calculated from

$$y^+ = \rho k^{1/2} C_\mu^{1/4} \delta / \mu_l \tag{14}$$

The inlet emission data, for reacting flows, has been taken from the measurements of a non-afterburner TF30-P-3 engine[15]. The predictions have been carried out with an overall fuel-air ratio of 0.008 and with a fuel flow rate of 0.037 kg/s. The temperature of the air and its axial velocity are taken to be 520 K and 200 m/s, respectively, at the film cooling slots. The walls of the liner are assumed to be cooled to the temperature of the inlet mixture (900 K for the present case). The fuel injector is assumed to be located at the inlet, upstream of the TRG apex and the fuel is assumed to be injected into the surrounding cells.

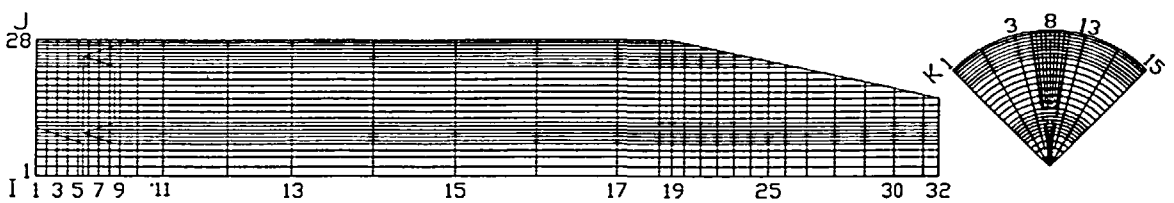

Figure 2 Grid network $32 \times 28 \times 15$

RESULTS AND DISCUSSION

The flow fields are presented in terms of vector plots to provide an overall assessment of the predicted flow patterns. Other properties are indicated as contour plots in longitudinal planes, in which the x and r coordinates indicate the axial and radial, respectively, coordinates in metres.

Isothermal flow fields

Figure 3 shows velocity vectors in the K=3 and 8 planes. In *Figure 3*(a), two ring gutters produce recirculation (RC) zones behind them, the lower one being longer due to the diffuser. The sharp-angled, cropped diffuser produces an anti-clockwise vortex near to it which gives better mixing behind BRG than TRG and it also provides energization of the adjacent region near the diffuser. The present location of the flame stabilizer completely eliminates the diffuser stall and flow separation losses. The large reverse flow near the centre is quite an important factor in assessing how far the reverse flow and the corresponding large scale eddies affect the unboosted thrust of the engine (non-afterburner conditions). The gradual acceleration of the flow inside the nozzle which gives the momentum thrust of the aircraft can be clearly seen. The velocities in the nozzle are maximum, giving an indication of the Mach number and the amount of variable nozzle opening which should be selected for the particular flow rate.

In *Figure 3*(b), the presence of RG gives different velocity profiles near the flame stabilizer because of the flow from the two trailing edges of the RG. This radially spread-out RC zone gives the flexibility of choosing the fuel injector orifices in spray-bar type fuel injection systems[16]. The length of the TRG RC zone has been increased and the negative u velocities are also comparatively high. This may be attributed to the increased velocities in betweeen ring gutters in *Figure 3*(a) which produce intense mixing with the top RC zone reducing its length. Although the differing flow patterns in *Figures 3*(a) and (b) can give rise to more radial and azimuthal transfer of momentum, the nozzle region indicates a similar pattern.

Figure 4 shows the cross-sectional plots at four different axial stations. In *Figure 4*(a), it is seen that, immediately downstream of the flame stabilizer (i.e., 8 mm from the edge), the axial velocity deficit regions behind the RG are compensated by the radial and azimuthal transfer of momentum, and the flow converges from both BRG and TRG. The anti-clockwise vortex pushes the flow upwards in the annular gap of the RG, producing more positive v velocities. The change

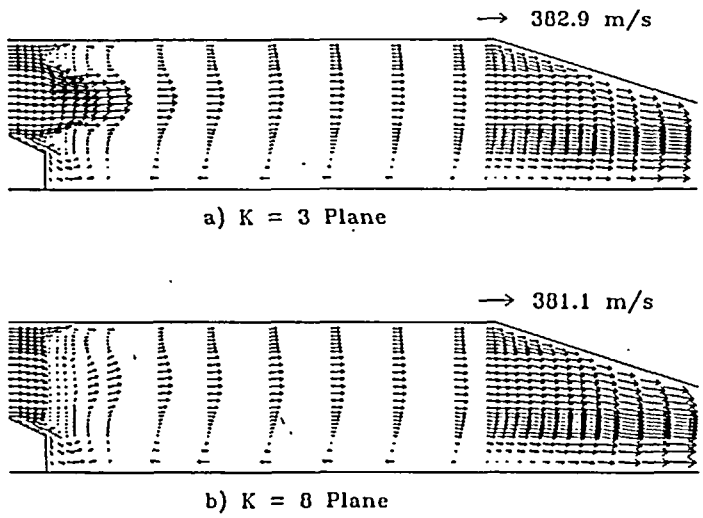

Figure 3 Longitudinal velocity vectors for isothermal flows

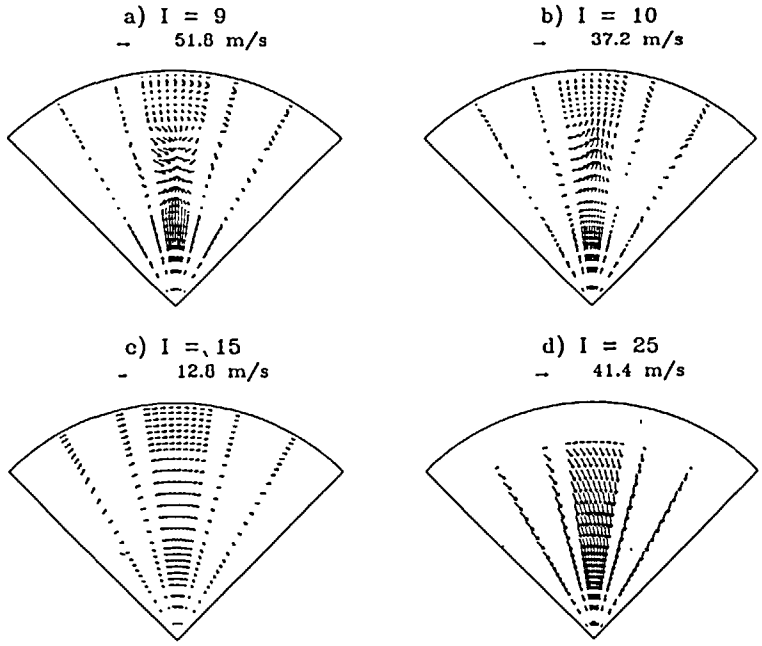

Figure 4 Cross-sectional velocity vectors for isothermal flows

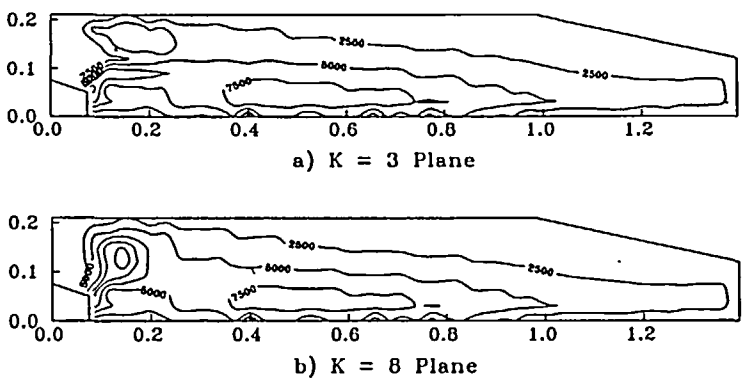

Figure 5 Turbulence kinetic energy contours of isothermal flows

in the direction of the vortex occurs between I=8 (not shown) and 9, as seen by observing the direction of v velocities near the centre. In *Figure 4*(b), at 36 mm from the edges of the flame stabilizer, the flow convergence from the two edges of TRG starts and the low is completely upwards downstream of the annular gap of the RG. The direction of the v velocities along the edges of RG is reverse compared to that of *Figure 4*(a). The flow becomes uniform in *Figure 4*(c), and there is a slight inward flow towards the negative u velocities near the centreline. In *Figure 4*(d), at I=25, which is inside the variable area nozzle, the converging nozzle effects can be clearly seen to increase the velocities considerably in all azimuthal planes. The magnitudes of the velocities near the centreline are smaller confirming the straight axial flow in *Figure 3*.

Figure 5 shows TKE contours in the K=3 and 8 planes. In *Figure 5*(a), the inlet TKE which is only 225 m^2/sec^2 increases by more than a factor of eleven just before the flame stabilizer,

due to the ring gutters. Two closed zones of intense TKE can be seen downstream of the two ring gutters in the RC zones and the TKE inside the annular V-regions is also very high. Within the RC zones, the velocities are low and the TKE is high which will help to anchor the flame and ensure proper combustion. In *Figure 5*(b), the RG spreads out the high TKE region radially and downstream of the RG where the flow converges as in *Figure 4*(a), the maximum TKE is seen. The negative velocities near the centreline produce intense turbulent fluctuations as can be seen in both *Figures 5*(a) and (b) and stretch the 5000 and 7500 m^2/sec^2 contours. Farther downsteam, the TKE is very small near the wall and a 2500 m^2/sec^2 contour exists in most of the afterburner flow regions.

Reacting flow fields

Figure 6 shows the velocity vector plots in the K = 3 plane for reacting flows. Large increases in velocities can be seen due to a decrease in density compared to *Figure 3*, though no converging nozzle is present. Two RC zones can be seen in *Figure 3*(a), but the large increase in velocities completely eliminates the lengthy RC zone and the negative u velocities near the centreline. Since the fuel injector is located upstream of the TRG, flow velocities increase due to combustion

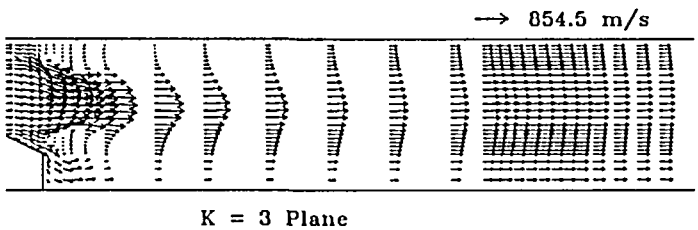

Figure 6 Longitudinal velocity vectors for reacting flows

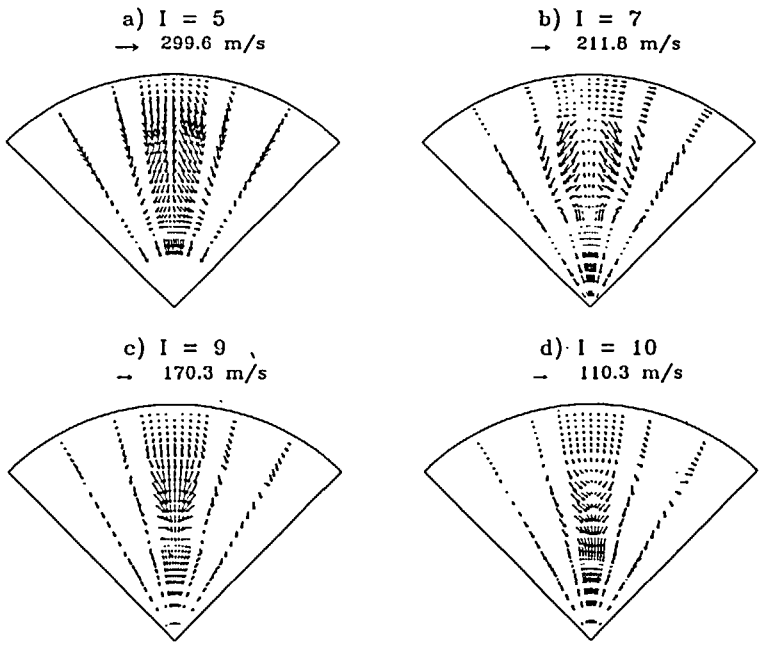

Figure 7 Cross-sectional velocity vector for reacting flows

in between ring gutters to the order of 855 m/s, producing a central-peaked velocity profile. Since combustion sharply accelerates the flow in between ring gutters, the flow over the upper face of the TRG is completely absent. This phenomenon in addition to the proximity of the TRG to the wall increases the length of the RC zone due to the TRG. Since the nozzle is assumed to be fully open, the velocities inside it are low; this may not be so in aircrafts because the nozzle opening is fixed depending upon the selected speed and fuel flow rate. The increase in the RC zone length due to the proximity to the wall[17] is confirmed by the increase in length behind the TRG; thus, providing stronger control over the RC zone length and, hence the geometry of the flame front.

Figure 7 shows the corresponding cross-sectional plots at four important axial stations. The flow patterns change completely from the inlet in *Figure 7*(a), just before the flame stabilizer. The maximum resultant velocity is of the order of 300 m/s; therefore, attention must be paid to the structural design of the flame stabilizer/fuel manifold ring assembly not only in the axial direction, but also in other directions. A strong, rigid fixing of the flame stabilizer inside the afterburner is essential. The bifurcation along the RG can be clearly seen to give rise to w velocities in opposite directions. In other azimuthal planes where the RG is not present, v velocities are predominant indicating the importance of the RG in creating swirl momentum. In *Figure 7*(b), almost half way across the flame stabilizer, only v velocities are present inside the RG since the RG is azimuthally constrained, and only w velocities are present inside the ring gutters since they are radially constrained. Since there is no flow along the upper face of the TRG, the fuel droplets/wall interaction might be eliminated. The bifurcation patterns in *Figures 7*(a) and (b) are exactly similar to those of isothermal flows except that the circumferential momentum is reduced compared with the radial one.

In *Figure 7*(c) at I=9, the mixing from two trailing edges of the RG is different from that of *Figure 4*(a), because of high v velocities in the central azimuthal planes produced by combustion. The transitions from negative v velocities at I=8 to positive at I=9 near the diffuser are similar in both cold and reacting flow situations. The flow is converging towards the central azimuthal plane behind the BRG and RG in *Figure 4*(a), whereas the flow along the edges of the RG is completely downward up to the upper lip of the BRG in *Figure 7*(c). The diverging flow patterns seen near the TRG in *Figure 4*(a) are replaced by fully downward flow. The flow convergence from the edges of the RG is still sharply downwards at I=10 compared to *Figure 7*(c). There is no upward flow behind the annular regions of the RG in *Figure 7*(d) as in *Figure 4*(b). Because of the increased RC zone length, there is no convergence of flow behind the TRG, whereas a clear convergence is seen behind the BRG. The flow convergence at I=10 behind the BRG and RG indicates high levels of turbulent mixing due to combustion. The free-stream flow in between the ring gutters in other than the RG azimuthal planes and the recirculation from RG interacting with a jet of trailing eddies of the mixing layer, enhance the interaction between combustion products and reactants and acts locally as a heat exchanger. The persistence of downward flow behind the edges of the RG at I=10 and the absence of upward flow along the upper face of the TRG may produce problems of droplet dripping near the edges of the flame stabilizer, thus giving high local equivalence ratio spots leading to combustion instabilities. Combustion instabilities occur mainly due to the unsteady heat release patterns which, of course, are related to the fuel distribution, and can cause mechanical failure in aircrafts. It has been found that low frequency combustion instabilities such as rumble and buzz are mainly produced by the fuel over-richness, particularly, near the flame stabilizer[2,18].

The different patterns of flow convergence downstream of the flame stabilizer due to combustion will have a major influence upon the fuel droplet trajectories after a certain period of afterburner operation. This will be very much helpful in the selection of fuel injection systems either of upstream type giving premixed flames (combustion peak at around equivalence ratio) or internal spray producing diffusion flames, so that combustion reaches its peak on the lean side. Also, the effects of juxtaposition of the fuel injector from the apex of V-gutter, on the amount of fuel captured by the gutters and mixing[19] can be better studied.

Reacting flow parameters

Turbulence kinetic energy: The TKE contours in *Figure 8*(a) show two high TKE regions near the BRG and TRG, and the TKE levels increase slowly in between the two ring gutters from their apex. The proximity to fuel injector location and increased RC zone length of the TRG produce very high, lengthy TKE zones compared to the BRG. A large increase in TKE levels of up to three times has been observed by Khalil[20]. This may be due to the decrease in the density of the gas with combustion which in turn increases the turbulence intensity. The increased turbulence fluctuations may be responsible for the increase in TKE with combustion. The absence of long bottom RC zone and the negative u velocities near the centreline eliminate the comparatively high TKE levels near the centreline downstream of the diffuser which can be seen in *Figure 5*(a).

Turbulence length scale: The turbulence length scale contours show a minimum near the flame stabilizer and increase to a maximum downstream progressively as shown in *Figure 8*(b). The length scales are useful to compare the sizes of the flame thickness and eddies.

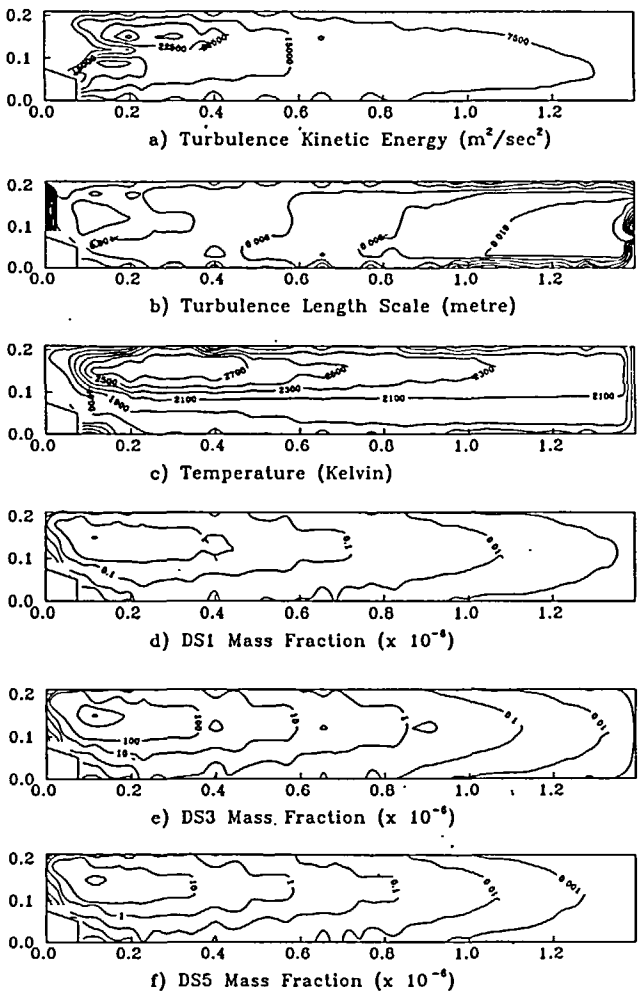

Figure 8 Reacting flow parameters in the $k=13$ plane

Temperature: The temperature increases monotonically from the inlet and reaches its maximum value downstream of the TRG as shown in *Figure 8*(c), where the top RC zone produces a lengthy flame front and a shear layer which fulfils all requirements for stable chemical reaction. It is fuel rich, has low velocities, contains hot gas products and has intensive mixing between fuel and air. Thus, a high degree of reaction can be observed near the TRG, whereas in the diffuser/BRG region, the temperature is comparatively low. Since there are no temperature limitations in afterburners as in combustors due to the presence of turbines, the maximum temperatures of the order of 2500 K in *Figure 8*(c) are allowed. A similar type of temperature increase reaching the maximum temperature of 2800 K (with inlet temperature of 1000 K) has also been observed by Raju and Sirignano[21] in a centrebody combustor. But the temperature near the wall has necessarily to be reduced which will be normally done in afterburners by means of a cooling liner. Normally, this will have a large number of holes through which air can be passed for cooling and also act as an effective 'screech' suppressor[16]. The large increase in temperature observed throughout the afterburner increases the velocity of the gases considerably to attain the required thrust boost. The contemporary advances made in materials technology results in increased turbine outlet temperatures and the corresponding high temperatures in the afterburner section necessitate advanced design of flame stabilizers like carburetting V-gutters, film vaporizing V-gutters and swirl-can modules[22] to meet the challenge of increased durability.

The increase in temperature near the inlet may be attributed to the assumption that the injected fuel is distributed only in the surrounding cells located near the injector. It would be more meaningful if the actual distribution of fuel in the afterburner were determined and the fuel distributed in cells properly chosen. Details regarding the distribution of fuel are not available and even if such details were available, a very fine grid arrangement would be required, hence, it was not attempted. Although the current predictions are mainly handicapped by the lack of spray dynamics analysis, since the assumed droplet sizes are very small (10–50 microns), the droplets will accelerate to values close to those of very high velocities of air and will exhibit similar velocity distributions. However, in the region near the injector, slip between the droplets and the surrounding gas phase must be properly accounted for in the droplet model to provide a satisfactory description of the spray near the injector.

Mass fractions of droplet sizes: Figures 8(d–f) show the contours of the mass fraction of droplets of three different sizes DS1, DS3 and DS5, i.e., the largest, medium and the smallest of the five droplet sizes assumed, respectively. The distributions of the three sizes are similar, though their values differ by orders of magnitude. The medium size droplets DS3 have the highest concentration, followed by the smallest size DS5 and the largest size DS1 in decreasing order. This ranking is mainly attributed to the initially prescribed Gaussian distribution and to the mathematical model employed which shows the larger droplets to decrease, i.e., growth is not considered. The concentrations of all sizes of droplets are highest near the fuel injector region with DS3 reaching 10^{-2}. The mass fractions of the DS1 and DS5 droplets become small, i.e., below 10^{-6} at 0.4–0.6 m of the afterburner, whereas DS3 droplets become 10^{-6} only at 0.8 m, i.e., downstream of the flame stabilizer, therefore the DS3 droplets exist to a large extent. Thus, if the fuel distribution in the cells near the fuel injector are properly chosen, the fuel spray capture by radial and ring gutters can be easily calculated. The mass fractions of all droplet sizes are very low near the diffuser/BRG and farther downstream. The above kind of distribution produced near the centreline and wall due to the fuel injector location gives rise to steep, radial temperature gradients, which may be undesirable for the interior afterburner components.

Unburnt fuel mass fraction: The rapid acceleration of the gases between the two ring gutters produces maximum velocities near the lower tip of TRG (cf. *Figure 6*), reducing the residence time. This results in high mass fractions of unburnt fuel and droplet sizes in that region. In *Figure 9*(a), the unburnt fuel in the annular and downstream regions of the TRG is comparatively low, showing a high degree of reaction. In the annular regions of the TRG, m_{fu} slowly decreases from the apex to the open edges indicating the progressive degree of reaction. Since the fuel

available for combustion near the diffuser and BRG itself is small, m_{fu} in those regions is very low, giving low temperatures in *Figure 8*(c). Further downstream, the fuel mass fraction is almost negligible, indicating the completeness of combustion. Thus, steep radial temperature gradients can be avoided by distributing the total fuel along different radial orifices in either a spray bar type or fuel manifold ring system.

O_2 mass fraction: Vigorous chemical reaction in the mixing zones formed by the lengthy RC zone of the TRG and the establishment of a stable flame by a balance of the continuing entrainment of cool unburnt gas and the heat and species transfer from the hot burnt gases are well indicated by the large depletion of oxygen downstream of the TRG in *Figure 9*(b). The reaction proceeds slowly from the apex to the lips of TRG due to the reduction in the oxygen mass fraction. This is because the space available for rapid exchange of burnt and unburnt gases increases slowly from the apex to the open edges of the TRG. Near the BRG and diffuser, since the fuel available for combustion itself is negligible, no reaction takes place and, hence, oxygen is available. The occurrence of reaction far downstream in the upper half of afterburner is well indicated by the reduction in oxygem mass fraction.

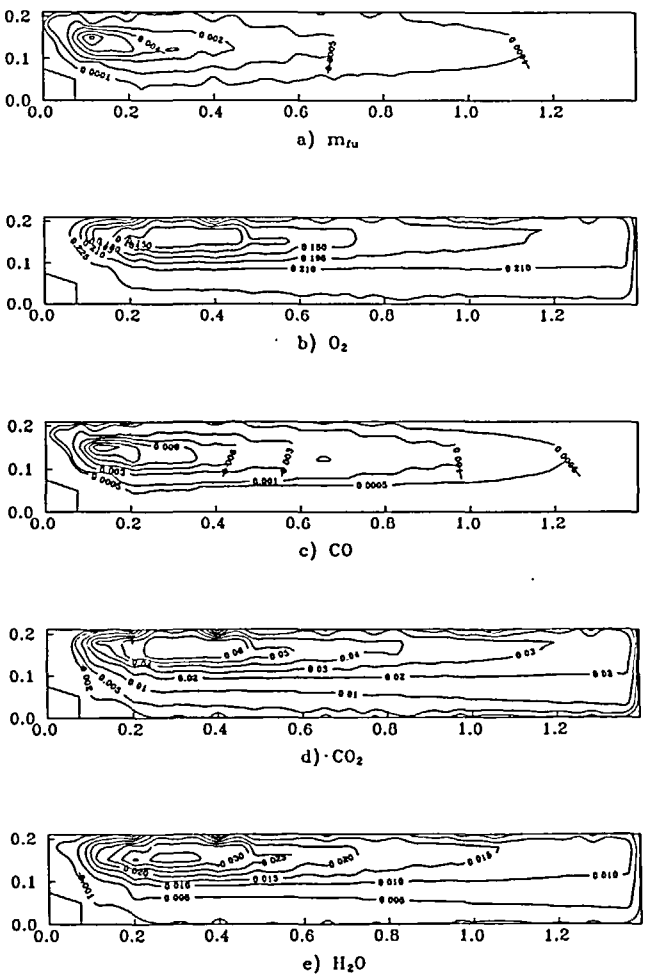

Figure 9 Species concentration in the $k=13$ plane

CO mass fraction: The CO mass fraction is high exactly at the same location where m_{fu} levels are high due to incomplete combustion in *Figure 9*(c). The CO mass fraction increases slowly from the inlet because combustion is slow in this region. Since more fuel is captured in the annular regions of the TRG and also the effective area near the apex inside the TRG is very small for the mixing of burnt and unburnt products, incomplete combustion takes place and more *CO* is present. The *CO* mass fractions far downstream are very low, indicating the completeness of combustion.

CO_2 and H_2O mass fractions: The high CO_2 and H_2O mass fraction regions in *Figures 9*(d) and (e) indicate the intense reaction zone which can be confirmed by the low O_2 levels in *Figure 9*(b). The increase in CO_2 and H_2O mass fractions in the annular regions of the TRG exactly correspond to the depletion of oxygen in the same region. Farther downstream, some amounts of CO_2 and H_2O are present, indicating the small degree of reaction. The diffuser/BRG regions remain almost reaction-free, and CO_2 and H_2O mass fractions are negligible. Comparisons of the contours of *CO*, CO_2 and H_2O indicate that the maximum *CO* concentration is of the same order as CO_2 and H_2O, i.e., 10^{-2}, which corresponds to an unoptimized location of the fuel injector.

Normally, for problems without transport, one differential equation must be solved for each of N chemical species, together with the energy equation, producing (N+1) equations. When transport effects are included, the same (N+1) equations must then be solved for each spatial zone, in addition to equations for conservation of mass and each component of momentum. For many typical applications, 30–40 spatial zones are needed in each dimension, so that 2-D and 3-D problems might contain 1000 and 30,000 zones respectively. Current reaction mechanisms for oxidation of methane or methanol contain 25–30 chemical species, so the use of these of fuels could require the solution of approximately 30, 1000, 35,000, and 1,000,000 coupled differential equations for zero-dimensional (no transport), 1-D, 2-D and 3-D models respectively according to a review by Westbrook and Dryer[23]. Also, well accepted detailed kinetics mechanisms are only available for a few low molecular weight fuels. Modelling the complete reaction sequence for the kerosene fuel selected, particularly, with a mixture of different species at the inlet is an impossible task when considering CPU time and memory. Hence, on making trade-offs between spatial scales, physical phenomena and chemical models, the accuracy of the chemical models has been compromised here. This is because, in the selected problem, the three-dimensional nature of the geometry is inherent and the fluid dynamics parameters are of main interest to us. Since chemical kinetics effects at high temperatures are not considered here, the effect of the inlet species concentrations on the overall distribution of species will not be exactly known. Although, considerable increase in CO_2 and H_2O mass fractions at the inlet can be seen, the impact of inlet species concentrations in such a simple reaction system cannot be effectively estimated.

CONCLUDING REMARKS

A finite volume procedure capable of calculating the flow and combustion processes within complex, three-dimensional geometries has been used to compute the aerodynamic flow fields, temperature and species concentrations within a turbojet afterburner. The results demonstrate the ability of the present method to predict the three-dimensional flow fields including eddies, recirculation patterns and mixing zones in both longitudinal and cross-sectional planes. The trends of the velocity profiles, elimination of duffuser stall and flow separation are more or less similar for both isothermal and reacting flows, justifying the importance of detailed cold flow analysis. However, the variations near the centreline and the converging flow patterns downstream of the flame stabilizer indicate the wide variety of flow situations expected to occur in afterburners for different periods of operation. The contours of temperature and species concentrations reveal that most of the reaction occurs near the top ring gutter, close to which the fuel injector is located. This indicates the need for rearranging the location of the fuel injector and placing it in an optimum position.

Unfortunately, there are no experimental data to compare the detailed flow fields and species concentrations. Such data will be helpful to validate the turbulence and combustion models. Although the eddy break-up model of Spalding has been extensively used in turbulent gaseous flames, its application to afterburners particularly with different species at the inlet, requires experimental validation. The physical model could be improved by taking into account the slip between the gas and the liquid, detailed chemical kinetics with more intermediate species of the combustion process and the effect of variable transport coefficients on the vaporization process, depending upon the computer resources available. The plausibility of the results obtained illustrates the potential of the method to provide a flexible analysis technique for turbujet afterburners.

REFERENCES

1 McAulay, J. E. and Abdelwahab, M. *Experimental evaluation of a TF30-P-3 turbofan engine in an altitude facility: afterburner performance and engine-afterburner operating limits*, NASA TN D-6839 (July 1972)
2 Cullom, R. R. and Johnsen, R. L. *Operating conditions and geometry effects on low-frequency afterburner combustion instability in a turbofan at altidude*, NASA TP-1475 (June 1979)
3 Sampath, S. and Ganesan, V. Experimental and theoretical investigations of flow behind bluff diodes, *J. Inst. Energy*, **213**, 213–234 (1981)
4 Yung, C. N., Keith, T. G. Jr. and Dewitt, K. J. Numerical prediction of cold turbulent flow in combustor configurations with different centerbody flameholders, *Paper No. ASME 86-WA/HT-50*, Anaheim, California (1986)
5 Lee, D. and Lin, J. S. Computation of nonreacting flows of a two-ring flame stabilizer using a zonal grid method, *Num. Heat Transfer*, Part A, **20**, 65–79 (1991)
6 Elgobashi, S., Pratt, D. T., Spalding, D. B. and Srivatsa, S. K. Unsteady combustion of fuel spray in jet engine afterburners, *Proc. 3rd Int. Symp. Air Breathing Engines*, Ed. F. S. Billig, Munich, Germany, AIAA Publications, 447–471 (1977)
7 Lixing, Z. and Jian, Z. Numerical modelling of turbulent evaporating gas-droplet two-phase flows in an afterburner diffuser of turbofan jet engines, *Chinese J. Aeronautics*, **3**, 258–265 (1990)
8 Zhang, X. and Chiu, H. Numerical modelling of afterburner combustion, *Int. J. Turbo and Jet Engines*, **4**, 251–262 (1987)
9 Chuang, S. H. and Jiang, J. S. Diffusion flame analysis of an afterburner as a function of the air-fuel ratio, *Int. J. Num. Methods. Fluids*, **11**, 303–316 (1990)
10 Isaac, J. J., Ramesh, N. R., Rajashekar, C., Shyamsundar, S. R., Baskaran, M. and Sivarmakrishna, G. Afterburner flow visualization studies in a water tunnel, *Proc. First National Conf. Air Breating Engines*, Bangalore, 121–128 (1992)
11 Launder, B. E. and Spalding, D. B. *Mathematical models of turbulence*, Academic Press, London, England (1972)
12 Spalding, C. B. Mathematical models of turbulent flames: A review, *Comb. Sci. Technol.*, **13**, 1–6, 3–25 (1976)
13 Patankar, S. V. and Spalding, D. B. A calculation procedure for heat, mass and momentum transfer in three-dimensional parabolic flows, *Int. J. Heat Mass Transfer*, **15**, 1787–1806 (1972)
14 Launder, B. E. and Spalding, D. B. The numerical computation of turbulent flows, *Comput. Methods. Appl. Mech. Engng.*, **3**, 269–289 (1974)
15 Diehl, L. A. *Preliminary investigation of gaseous emissions from jet engine afterburners*, NASA TM X-2323 (1971)
16 Lundin, B. T., Gabriel, D. S. and Fleming, W. A. *Summary of NACA research on afterburners for turbujet engines*, NACA RM E55L12 (1956)
17 Ravichandran, M. and Ganesan, V. Aerodynamic flow investigations in an isothermal model of an afterburner. *Experiments in Fluids*, **17**, 1/2, 59–67 (1994)
18 Sotheran. A. *High performance turbofan afterburner systems*, AGARD CP-422, pp. 12.1–12.9 (1988)
19 Cao, M. H. and Chin, J. S. Further study on the prediction of liquid fuel spray capture by V-gutter downstream of a plain orifice injector under uniform cross air flow, *Proc. 6th Int. Symp. Air Breathing Engines*, Ed. F. S. Billig, Paris, France, AIAA Publications, 64–72 (1983)
20 Khalil, E. E., Spalding, D. B. and Whitelaw, J. H. The calculation of local flow properties in two-dimensional furnaces, *Int. J. Heat Mass Transfer*, **18**, 775–791 (1975)
21 Raju, M. S. and Sirignano, W. A. Spray computations in a centerbody combustor, *Trans. ASME J. Engg. Gas Turbines and Power*, **111**, 710–718 (1989)
22 Reck, G. M., Branstetter, J. R. and Diehl, L. A. *Preliminary sector tests at 920 K (1200°F) of three afterburner concepts applicable for higher inlet temperatures*, NASA TN D-6437 (1971)
23 Westbrook, C. K. and Dryer, F. L. Chemical kinetic modelling of hydrocarbon combustion, *Prog. Energy Combust. Sci.*, **10**, 1–57 (1984)